THE UNIVERSITY *of* EDINBURGH

Edinburgh Research Explorer

Time sequence learning for electrical impedance tomography using Bayesian spatiotemporal priors

OPEN ACCESS

Efficient Multi-Task Structure-Aware Sparse Bayesian Learning for Frequency-Difference Electrical Impedance Tomography

Shengheng Liu, *Member, IEEE*, Yongming Huang, *Senior Member, IEEE*, Hancong Wu, *Member, IEEE*, Chao Tan, *Senior Member, IEEE*, and Jiabin Jia, *Senior Member, IEEE*

Abstract—Frequency-difference electrical impedance tomography (fdEIT) was originally developed to mitigate the systematic artifacts induced by modeling errors when a baseline data set is unavailable. Instead of fine anatomical imaging, only coarse anomaly detection has been addressed in current fdEIT research mainly due to its low spatial resolution. On the other hand, there has been not much study on fdEIT reconstruction algorithm as well. In this paper, we propose an efficient and high-spatial-resolution algorithm for simultaneously reconstructing multiple fdEIT frames corresponding to inject currents with multiple frequencies. The EIT reconstruction problem is considered within a hierarchical Bayesian framework, where both intra-task spatial clustering and inter-task dependency are automatically learned and exploited in an unsupervised manner. The computation is accelerated by adopting a modified marginal likelihood maximization approach. Real-data experiment are conducted to verify the recovery performance of the proposed algorithm.

Index Terms—Inverse problem, electrical impedance tomography (EIT), sparse Bayesian learning (SBL), image reconstruction, frequency difference.

I. INTRODUCTION

THE reconstruction problem in electrical impedance tomography (EIT) is to determine the spatially-varying conductivity distribution inside an object given the boundary current-voltage measurements. As an emerging agile tomographic imaging technique and compared with other popular imaging modalities [1], [2], EIT shows immense potential in medical applications due to its *in vivo* and *in situ* capabilities,

which can be exploited in understanding the physiological dynamics and pathological conditions. EIT imaging techniques can be divided into two categories, i.e., static and differential imaging [3]. The goal of static imaging is to recover the absolute conductivity distribution based on the data set from a single voltage measurement, which generally suffers from systematic artifacts resulted from various modeling error sources such as boundary geometry, electrode positions, body movement, and inter-individual anatomy [3], [4]. Differential imaging, in contrast, reconstructs the changes in the conductivity by inferring from the difference between two measured states [5], where the systematic artifacts can be readily reduced through measurement cancellation.

While the overwhelming majority of EIT clinical images have been produced using time-difference data, frequency-difference EIT (fdEIT) has received fewer attention in the literature and is at an earlier stage of development [6]–[10]. fdEIT uses voltage data sets with multiple excitation frequencies to calculate an image of the corresponding changes of conductivity. As such, not only is it capable of effectively eliminating common boundary geometry errors as in time-difference EIT (tdEIT) [11], it also allows for removing body movement induced artifacts provided data collection is fast. In addition, fdEIT is more suitable for breast tumor or stroke type classification, where time reference data are not available, and frequency-dependent conductivity spectra of specific tissues are able to provide additional diagnostic information to current EIT systems [10]–[12]. However, as changes of conductivity with frequency are generally insignificant compared with conductivity changes during a moderate time interval in tdEIT, the measurements in fdEIT are very sensitive to noise [13]. Another well-known drawback of fdEIT is the inherent low spatial resolution. In regard to this, previous research on fdEIT mainly focuses on anomaly detection instead of imaging [14].

To counteract the severe ill-poseness and constrain the solution of fdEIT, structural *a priori* knowledge can be incorporated to rule out the wild variations behind the instability. One natural and convenient mechanism to accomplish this is to employ Bayesian approaches [15], [16], which are aimed to characterize the posterior distribution, e.g., computing posterior moments or other posterior expectations. Sparse Bayesian learning (SBL) framework has drawn much attention due to its unique capability to flexibly modelling and adaptively explore exploit underlying data structures. In addition, SBL is more advantageous than other competitive signal recovery

algorithms in the sense that it is more robust in noisy environments, and offers better performance when the columns of the dictionary matrix are highly correlated and/or the image to be reconstructed is not highly sparse [17], which is particularly attractive to EIT applications.

In some recent works [18], [19], EIT image reconstruction was formulated as a Bayesian statistical inversion problem [20], [21], and a novel structure-aware sparse Bayesian learning (SA-SBL) based method was presented to obtain an significantly improved spatial resolution. In this paper, we expand upon the SA-SBL algorithm for difference EIT imaging, and consider fast multiple frame reconstruction. High temporal resolution of EIT benefits practical applications but also results in massive frames to be reconstructed. To facilitate, for example, low-cost and prompt-response early stroke diagnosis in emergency scenarios, more efficient algorithm is in high demanding. The contributions of this work on the basis of the recent work in [18], [19] is fourfold: (a) fdEIT image reconstruction is investigated within the multiple measurement vector (MMV) SBL framework, which is fundamentally different from the single measurement vector problem in [18], [19]; (b) The inter-task dependency between frames with different frequencies is considered to yield an enhanced recovery performance; (c) Instead of derive the maximum *a posteriori* (MAP) estimates using expectation maximization (EM) method, we employ an efficient marginal likelihood maximization (MLM) approach to achieve much more efficient computation. (d) Two measurable metrics based on regional relative cardinalities are designed to draw a objective and quantitative comparison of the competitive methods.

Following this introductory section, Section II presents the signal model used in this paper. Section III then elaborates the proposed sequential reconstruction algorithm based on multi-task structure-aware sparse Bayesian learning (MT-SA-SBL). The experimental results using real collected data is provided in Section IV. The paper is concluded in Section V.

Notations: Lower-case (/upper-case) bold characters are used to denote vectors (/matrices). $\bar{(\cdot)}$ and $|\cdot|$ respectively return the average of a given vector and the modulus of a given complex number. $\text{diag}\{\mathbf{A}\}$ returns a column vector consisting of the main diagonal entries, whereas and $\text{diag}\{\mathbf{A}, 1\}$ returns one corresponding to the first-diagonal entries above the main diagonal. $\mathbf{I}_N$ denotes an $N \times N$ identity matrix. $\text{tr}(\cdot)$ and $(\cdot)^{\top}$ respectively represent the trace and transpose operation of a matrix. $\|\cdot\|_p$ represents the ℓ_p-norm of a vector, and $\|\cdot\|_F$ represents the Frobenius norm of a matrix. $\mathbb{E}(\cdot)$ returns the expected value of a discrete random variable. $p(\cdot)$ denotes the probability density function. $\mathcal{N}(\cdot)$ denotes Gaussian distribution. $\mathbb{R}$ is the set of real numbers. $\cup$ and $\cap$ respectively denote union and intersection of two sets. $\text{card}\{\cdot\}$ returns the cardinality of a set.

II. PROBLEM FORMULATION

In fdEIT, it is essential to use the weighted voltage difference between two frequencies to produce an image of frequency-dependent changes of the internal conductivity distribution [11]. In doing so, the conductivity change of background substance is suppressed while the magnitude of inclusion is enhanced. The weighted normalization form can be expressed as

$$\delta\mathbf{y} = \left(\mathbf{y}_{\omega_2} - \alpha\mathbf{y}_{\omega_1}\right) / \left(\alpha\mathbf{y}_{\omega_1}\right), \tag{1}$$

where α is a weight which equals to the inner product ratio between two voltages vectors at different frequency:

$$\alpha = \langle\mathbf{y}_{\omega_2}, \mathbf{y}_{\omega_1}\rangle / \langle\mathbf{y}_{\omega_1}, \mathbf{y}_{\omega_1}\rangle. \tag{2}$$

Typically, the following linear approximation is used to relate the internal conductivity changes $\delta\boldsymbol{\kappa} \in \mathbb{R}^{N \times 1}$ to the corresponding boundary voltage changes $\delta\mathbf{y} \in \mathbb{R}^{M \times 1}$ ($M < N$):

$$\delta\mathbf{y} = \mathbf{J}\delta\boldsymbol{\kappa}, \tag{3}$$

where $\mathbf{J} \in \mathbb{R}^{M \times N}$ is the sensitivity matrix, a matrix defined by mesh, electrode positions and current injection and measurement protocol. An extension of the inverse model described in (3) for simultaneously recovering EIT images from multiple-frequency channels can be expressed as

$$\delta\mathbf{Y} = \mathbf{J}\delta\mathbf{K}, \tag{4}$$

where $\delta\mathbf{Y}$ is an $M \times L$ matrix containing the multiple-frequency measurement vectors $\delta\mathbf{Y}_{:,l}$ of size $M \times 1$, and $\delta\mathbf{K}$ is an $N \times L$ matrix containing the solution images $\delta\mathbf{K}_{:,l}$ of size $N \times 1$. ($l = 1, 2, \ldots, L$, and L is the number of channels to be recovered.) This extended model is termed MMV model in compressive sensing community.

For notational convenience, in the following discussion, we simplify the notations $\delta\mathbf{K}$ and $\delta\mathbf{Y}$ as $\mathbf{K}$ and $\mathbf{Y}$, respectively. In addition, we also include additive noise matrix with i.i.d. Gaussian entries $\mathbf{V} \sim \mathcal{N}\left(\mathbf{0}, \gamma_0\mathbf{I}\right)$ in the signal model. Now (4) is simplified as

$$\mathbf{Y} = \mathbf{J}\mathbf{K} + \mathbf{V}. \tag{5}$$

As depicted in Fig. 1, we assume in this work that all reconstructed EIT images in different frequency channels share similar or identical sparse support, i.e., inter-channel correlation exists, which is a reasonable assumption in EIT since the variations of pixel amplitudes are moderate among different frequency channels. On the other hand, the non-zero entries in each channel are also assumed to exhibit intra-channel clustering. Note that as shown in Fig. 1, the neighborhood entries in the frames are not necessarily mutually adjacent in the reconstructed conductivity matrix $\mathbf{K}$. Therefore, a mapping module is required to automatically find the dependent pixels for each pixel under investigation. To solve the SMV problem formulated in (3), a single conductivity solution vector $\delta\boldsymbol{\kappa}$ is reconstructed from the single voltage measurement vector $\delta\mathbf{y}$. By comparison, in this work, we consider simultaneously recovering multiple EIT frames in multiple-frequency channels. Accordingly, all the voltage measurement vectors from different frequency channels constitute a measurement matrix $\delta\mathbf{Y}$. Now the task turns into reconstructing the solution matrix $\mathbf{K}$ (right hand side of Fig. 1) comprised of multiple EIT frames from the measurement matrix, which becomes an MMV problem.

For we have no *a priori* knowledge on the intra-channel clustering partition pattern, by following the methodology in
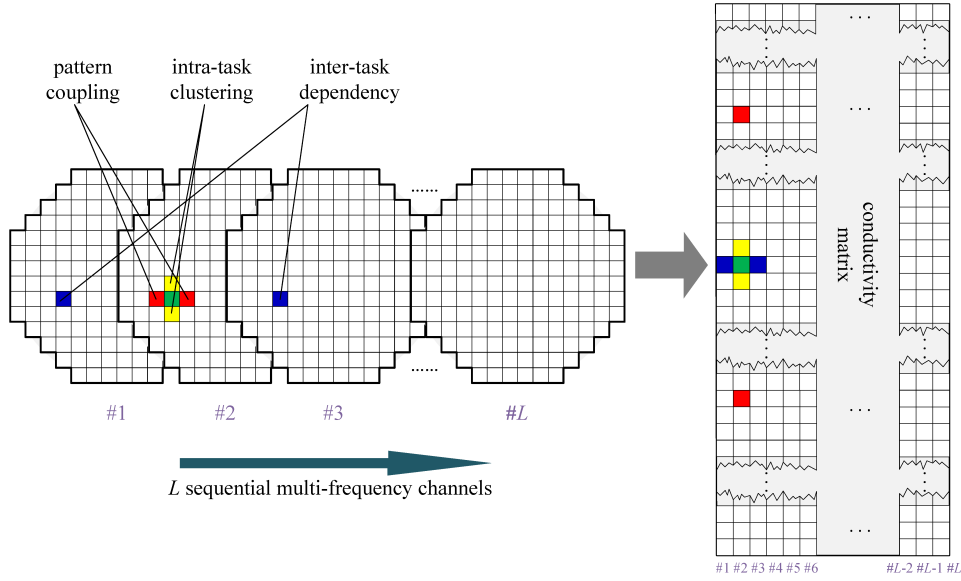
Fig. 1. Illustration of continuous structure considered in the fdEIT signal model.

the related work [18], we consider overlapping clusters with an equal size h and arbitrarily distributed nonzero entries, and the real pattern is learned by revoking and merging the preset clusters during the SBL process. To facilitate the utilization of SA-SBL framework, we factorize the l-th column of $\mathbf{K}$ as

$$\mathbf{K}_{:,l} \triangleq \mathbf{\Psi}\mathbf{X}_{:,l} \triangleq \left[\mathbf{\Psi}_{:,[1]}, \ldots, \mathbf{\Psi}_{:,[g]}\right] \left[\mathbf{X}_{[1],l}^\top, \ldots, \mathbf{X}_{[g],l}^\top\right]^\top, \quad (6)$$

where $g = N - h + 1$ is the total number of clusters. In addition, for $\forall i = 1, 2, \ldots, g$, $\mathbf{X}_{[i],l} = [x_{i,l}, \ldots, x_{i+h-1,l}]^\top \in \mathbb{R}^{h \times 1}$ denotes the i-th preset cluster, and $\mathbf{\Psi}_{:,[i]} \triangleq \left[\mathbf{0}_{(i-1)\times h}^\top, \mathbf{I}_{h \times h}^\top, \mathbf{0}_{(N-i-h+1)\times h}^\top\right]^\top \in \mathbb{R}^{N \times h}$. The underlying linear model in (5) can then be rewritten as

$$\mathbf{Y} = \mathbf{J}\mathbf{\Psi}\mathbf{X} + \mathbf{V} \triangleq \mathbf{\Phi}\mathbf{X} + \mathbf{V}. \quad (7)$$

For the sake of consistency with our previous work [18], we still assume $\left\{\mathbf{B}_i \in \mathbb{R}^{h \times h}\right\}_{i=1}^{g}$ controls the intra-channel block structure. In addition, $\mathbf{A} \in \mathbb{R}^{L \times L}$ is defined to capture the inter-channel correlation in each row of $\mathbf{X}$. Then, the prior of the vectorized weights $\text{vec}(\mathbf{X}^\top)$ follows a zero-mean Gaussian distribution with $\text{vec}(\mathbf{X}^\top) \sim \mathcal{N}(\mathbf{0}, \mathbf{\Sigma}_0 \otimes \mathbf{A})$, where the stretched covariance matrix is expressed as $\mathbf{\Sigma}_0 = \text{diag}\{\gamma_1\mathbf{B}_1, \ldots, \gamma_g\mathbf{B}_g\} \in \mathbb{R}^{gh \times gh}$. In modelling the group sparsity, independent hyperparameter for each group is used to moderate the strength of the prior. The vectorized noise matrix $\text{vec}(\mathbf{V}^\top)$ is assumed to follow the distribution $\text{vec}(\mathbf{V}^\top) \sim \mathcal{N}(\mathbf{0}, \gamma_0\mathbf{I} \otimes \mathbf{A})$.

III. SEQUENTIAL RECONSTRUCTION ALGORITHM

Directly reconstructing unknowns in the inverse model (7) can lead to very inefficient estimation because of the mutual coupling between $\mathbf{A}$ and $\mathbf{B}_i$. This problem can be tackled by adopting the switching-learning approach [22], i.e., whitening towards one before estimating another, and then perform the other way around. We first whiten the inverse model towards

the matrix $\mathbf{A}$ that controls the inter-channel correlation. To this end, let $\widetilde{\mathbf{Y}} = \mathbf{Y}\mathbf{A}^{-1/2}$, $\widetilde{\mathbf{X}} = \mathbf{X}\mathbf{A}^{-1/2}$, $\widetilde{\mathbf{V}} = \mathbf{V}\mathbf{A}^{-1/2}$. Therefore, the prior probability distributions of the whitened model become $\widetilde{\mathbf{X}} \sim \prod_{l=1}^{L} \mathcal{N}(\mathbf{0}, \mathbf{\Sigma}_0)$ and $\widetilde{\mathbf{V}} \sim \prod_{l=1}^{L} \mathcal{N}(\mathbf{0}, \gamma_0\mathbf{I})$. Thus, the *a posteriori* belief for the l-th column of the whitened weights $\widetilde{\mathbf{X}}$ is subject to the following Gaussian distribution

$$p\left(\widetilde{\mathbf{X}}_{:,l} \middle| \widetilde{\mathbf{Y}}_{:,l}; \Theta\right) = \mathcal{N}\left(\boldsymbol{\mu}_{:,l}, \mathbf{\Sigma}\right), \quad (8)$$

where $\Theta \triangleq \{\gamma_0, \{\gamma_i, \mathbf{B}_i\}_{i=1}^{g}\}$ denotes the hyperparameters with mean vector

$$\boldsymbol{\mu}_{:,l} = \mathbf{\Sigma}_0\mathbf{\Phi}^\top\left(\gamma_0\mathbf{I} + \mathbf{\Phi}\mathbf{\Sigma}_0\mathbf{\Phi}^\top\right)^{-1}\widetilde{\mathbf{Y}}_{:,l}, \quad (9)$$

and covariance matrix

$$\mathbf{\Sigma} = \left(\mathbf{\Sigma}_0^{-1} + \frac{1}{\gamma_0}\mathbf{\Phi}^\top\mathbf{\Phi}\right)^{-1} = \mathbf{\Sigma}_0 - \mathbf{\Sigma}_0\mathbf{\Phi}^\top\mathbf{C}^{-1}\mathbf{\Phi}\mathbf{\Sigma}_0, \quad (10)$$

with

$$\mathbf{C} \triangleq \gamma_0\mathbf{I} + \mathbf{\Phi}\mathbf{\Sigma}_0\mathbf{\Phi}^\top \in \mathbb{R}^{M \times M}. \quad (11)$$

The MAP probability estimate of $\mathbf{X}$ in the original model (7) is obtained from the estimated posterior mean as $\mathbf{X} \leftarrow \boldsymbol{\mu}\mathbf{A}^{1/2}$, prior to which, the hyperparameters Θ must be estimated first. We use the following logarithmic cost function as in [18]:

$$\mathcal{L}(\Theta) = \log|\mathbf{C}| + \sum_{l=1}^{L} \widetilde{\mathbf{Y}}_{:,l}^\top\mathbf{C}^{-1}\widetilde{\mathbf{Y}}_{:,l}. \quad (12)$$

The improved efficiency of the proposed method is achieved by conditioning the marginal likelihood on an individual hyperparameter associated with the group under investigation, which significantly reduces the problem dimension. Concretely, we rewrite $\mathbf{C}$ from (11) in a convenient form to analyze

the dependence on group i ($i = 1, \ldots, g$):

$$
\begin{aligned}
\mathbf{C} &= \gamma_0 \mathbf{I} + \sum_j \gamma_j \boldsymbol{\Phi}_{:,[j]} \boldsymbol{\Phi}_{:,[j]}^\top \\
&= \left(\gamma_0 \mathbf{I} + \sum_{j \neq i} \gamma_j \boldsymbol{\Phi}_{:,[j]} \boldsymbol{\Phi}_{:,[j]}^\top \right) + \gamma_i \boldsymbol{\Phi}_{:,[i]} \boldsymbol{\Phi}_{:,[i]}^\top \\
&= \mathbf{C}_{\backslash i} + \gamma_i \boldsymbol{\Phi}_{:,[i]} \boldsymbol{\Phi}_{:,[i]}^\top,
\end{aligned}
\tag{13}
$$

where $\mathbf{C}_{\backslash i}$ is defined as the covariance matrix without the influence of basis $\boldsymbol{\Phi}_{:,[i]}$. By using established matrix determinant and Woodbury identity, the cost function (12) is pruned to the following form:

$$
\mathcal{L}(\Theta) = \log |\mathbf{I} + \gamma_i \mathbf{B}_i \mathbf{S}_i| - \mathbf{Q}_i^\top \left((\gamma_i \mathbf{B}_i)^{-1} + \mathbf{S}_i \right)^{-1} \mathbf{Q}_i, \tag{14}
$$

where $\mathbf{S}_i \triangleq \boldsymbol{\Phi}_{:,[i]}^\top \mathbf{C}_{\backslash i}^{-1} \boldsymbol{\Phi}_{:,[i]} \in \mathbb{R}^{h \times h}$ and $\mathbf{Q}_i \triangleq \boldsymbol{\Phi}_{:,[i]}^\top \mathbf{C}_{\backslash i}^{-1} \widetilde{\mathbf{Y}} \in \mathbb{R}^{h \times L}$. To avoid the exhaustive matrix inversion of $\mathbf{C}_{\backslash i}^{-1}$ with i varying from 1 to g, we first obtain $\mathbf{C}^{-1}$ from (11) using Woodbury identity as

$$
\mathbf{C}^{-1} = \gamma_0^{-1} \mathbf{I} - \gamma_0^{-2} \boldsymbol{\Phi} \boldsymbol{\Sigma} \boldsymbol{\Phi}^\top. \tag{15}
$$

Then we replace the term $\mathbf{C}_{\backslash i}^{-1}$ with $\mathbf{C}^{-1}$ in the definition of $\mathbf{S}_i$ and $\mathbf{Q}_i$, i.e.,

$$
\begin{aligned}
\tilde{\mathbf{S}}_i &\triangleq \boldsymbol{\Phi}_{:,[i]}^\top \mathbf{C}^{-1} \boldsymbol{\Phi}_{:,[i]} \\
&= \gamma_0^{-1} \boldsymbol{\Phi}_{:,[i]}^\top \boldsymbol{\Phi}_{:,[i]} - \gamma_0^{-2} \boldsymbol{\Phi}_{:,[i]}^\top \boldsymbol{\Phi} \boldsymbol{\Sigma} \boldsymbol{\Phi}^\top \boldsymbol{\Phi}_{:,[i]}
\end{aligned}
\tag{16}
$$

and

$$
\begin{aligned}
\tilde{\mathbf{Q}}_i &\triangleq \boldsymbol{\Phi}_{:,[i]}^\top \mathbf{C}^{-1} \widetilde{\mathbf{Y}} \\
&= \gamma_0^{-1} \boldsymbol{\Phi}_{:,[i]}^\top \widetilde{\mathbf{Y}} - \gamma_0^{-2} \boldsymbol{\Phi}_{:,[i]}^\top \boldsymbol{\Phi} \boldsymbol{\Sigma} \boldsymbol{\Phi}^\top \widetilde{\mathbf{Y}}.
\end{aligned}
\tag{17}
$$

Assume that the matrix $\tilde{\mathbf{S}}_i$ can be factorized as $\tilde{\mathbf{S}}_i = \mathbf{P}_i \text{diag}(s_{i,k}) \mathbf{P}_i^\top$, where $\mathbf{P}_i$ represents the eigenmatrix of $\tilde{\mathbf{S}}_i$, and $s_{i,k}$, ($k = 1, \ldots, h$) denotes the k-th eigenvalue of $\tilde{\mathbf{S}}_i$. We can then obtain $\mathbf{S}_i$ and $\mathbf{Q}_i$ by using the eigenvalue decomposition of $\tilde{\mathbf{S}}_i$ as

$$
\mathbf{S}_i = \mathbf{P}_i \text{diag} \left(\frac{s_{i,k}}{1 - \gamma_i s_{i,k}} \right) \mathbf{P}_i^\top \tag{18}
$$

and

$$
\mathbf{Q}_i = \mathbf{P}_i \text{diag} \left(\frac{1}{1 - \gamma_i s_{i,k}} \right) \mathbf{P}_i^\top \tilde{\mathbf{Q}}_i. \tag{19}
$$

The updating rules for the hyperparameters can be obtained by setting their corresponding derivative of (14) to zero. Similar to [18], regularization is introduced to avoid the overfitting problem, where $\mathbf{B}_i$ is updated by averaging an intermediate variable $\widehat{\mathbf{B}}_i$, i.e.,

$$
\widetilde{\mathbf{B}}_i^{\text{new}} = \widetilde{\mathbf{B}}_i + \frac{1}{\gamma_i L} \sum_{l=1}^{L} \left(\mathbf{S}_i^{-1} \left(\mathbf{Q}_{i,l} \mathbf{Q}_{i,l}^\top - \mathbf{S}_i \right) \mathbf{S}_i^{-1} \right), \tag{20}
$$

where $\mathbf{Q}_{i,l}$ represents the l-th column of $\mathbf{Q}_i$. A robust estimation of $\mathbf{B}_i$ is then obtained by constraining it to the following Toeplitz form:

$$
\mathbf{B}_i^{\text{new}} = \frac{\text{Toeplitz} \left([r_i^0, r_i^1, \ldots, r_i^{h-1}] \right)}{\left\| \text{Toeplitz} \left([r_i^0, r_i^1, \ldots, r_i^{h-1}] \right) \right\|_F} \tag{21}
$$

where

$$
r_i = \text{sign}(\tilde{r}_i) \cdot \min \{ |\tilde{r}_i|, 0.99 \}, \tag{22}
$$

$$
\tilde{r}_i = \frac{\overline{\text{diag}(\widetilde{\mathbf{B}}_i, 1)}}{\overline{\text{diag}(\widetilde{\mathbf{B}}_i)}}. \tag{23}
$$

Also taking into account the pattern coupling between the hyperparameter γ_i and the hyperparameters $\{\gamma_{i+}, \gamma_{i-}\}$ of its neighboring clusters, where subscripts $i+$ and $i-$ respectively indicate the neighboring clusters of the i-th cluster with larger and smaller indices, the updating rule for γ_i can be derived as

$$
\begin{aligned}
\gamma_i^{\text{new}} = \frac{1}{hL} (\gamma_i + \beta \gamma_{i+} + \beta \gamma_{i-}) \cdot \\
\sum_{l=1}^{L} \text{tr} \left(\mathbf{B}_i^{-1} \mathbf{S}_i^{-1} \left(\mathbf{Q}_{i,l} \mathbf{Q}_{i,l}^\top - \mathbf{S}_i \right) \mathbf{S}_i^{-1} \right).
\end{aligned}
\tag{24}
$$

We can also obtain the updating rule for γ_0 as

$$
\gamma_0 = \frac{1}{ML} \left\| \widetilde{\mathbf{Y}} - \boldsymbol{\Phi} \boldsymbol{\mu} \right\|_F^2 + \frac{1}{M} \sum_{i=1}^{g} \text{tr} \left(\boldsymbol{\Sigma}_{[i]} \boldsymbol{\Phi}_{:,[i]}^\top \boldsymbol{\Phi}_{:,[i]} \right). \tag{25}
$$

Similarly, matrix $\mathbf{A}$ can be estimated by whitening the inverse model towards $\mathbf{B}$. The resulting updating rule for $\mathbf{A}$ is given as follows

$$
\widetilde{\mathbf{A}}^{\text{new}} = \frac{(\mathbf{Y} - \boldsymbol{\Phi} \mathbf{X})^\top (\mathbf{Y} - \boldsymbol{\Phi} \mathbf{X})}{\gamma_0} + \sum_{i=1}^{g} \frac{\mathbf{X}_{[i],:}^\top \mathbf{B}_i^{-1} \mathbf{X}_{[i],:}}{\gamma_i}, \tag{26}
$$

$$
\mathbf{A}^{\text{new}} = \frac{\widetilde{\mathbf{A}}}{\left\| \widetilde{\mathbf{A}} \right\|_F}. \tag{27}
$$

A pseudo-code implementation of the proposed MT-SA-SBL-based algorithm for EIT image reconstruction is provided in **Algorithm 1**. In initializing **Algorithm 1**, parameters $\epsilon_{\min}$ and $\vartheta_{\max}$ are selected according to the accuracy and runtime constraints. As suggested in [18], we set $h = 4$ and $\beta = 0.25$. Other initial values such as γ_0 and $\mathbf{B}_i$ are empirically chosen according to extensive numerical simulations, which has little impact on the algorithm performance since they will be learned and altered afterwards.

Remark 1: It is worth pointing out that, in the proposed algorithm, if any $\gamma_i = 0$, its corresponding basis $\boldsymbol{\Phi}_{:,[i]}$ is excluded from the current model. For in a sparse recovery generally most of γ_i is zero, only a small fraction of the g clusters contribute to the computational load. Hence, the overall computational complexity is reduced since it heavily depends on the size of the utilized basis set in each iteration. With the parameter settings in our experiment, the proposed algorithm in this paper can achieve a speedup ratio of ~ 10 in comparison with EM-based approach.

IV. EXPERIMENT RESULTS AND DISCUSSIONS

The proposed MT-SA-SBL-based algorithm was tested against the real recorded data from a planar wideband EIT sensor system designed to monitor biological process named SWEIT [23]. The SWEIT system integrates 16 electrodes to realize excitation and measurement over 1 kHz – 1.1 MHz. The average signal-to-noise ratio is 56 dB in each channel and a good consistency is achieved. A photograph taken during the phantom experiment is shown in Fig. 2(a). The internal diameter and height of the sensor are respectively 125 mm

Algorithm 1: Pseudo-code for fdEIT image reconstruction based on MT-SA-SBL algorithm.

Input : $\mathbf{Y}$, $\mathbf{J}$, h, β, $\epsilon_{\min}$, $\vartheta_{\max}$

Initialize : Set $\epsilon = 1$, $\vartheta = 0$, $\boldsymbol{\mu} = \mathbf{0}_{gh \times L}$,

$\quad\quad\quad \boldsymbol{\Sigma} = \mathbf{0}_{gh \times gh}$, $\gamma_i = \mathbf{1}_{g \times 1}$,

$\quad\quad\quad \gamma_0 = \frac{0.01}{L} \times \sum\limits_{l=1}^{L} \sqrt{\frac{1}{M-1} \sum\limits_{i=1}^{M} |y_{i,l} - \bar{\mathbf{y}}_{:,l}|^2}$,

$\quad\quad\quad \mathbf{B}_i = \mathrm{Toeplitz}([0.9^0, \ldots, 0.9^{h-1}])$.

Iterations:

1 **while** $\epsilon > \epsilon_{\min}$ and $\vartheta \le \vartheta_{\max}$ **do**

2 $\quad$ Update $\mathbf{A}$ using (26), (27);

3 $\quad$ Update $\boldsymbol{\mu}_{:,l}$ using (9);

4 $\quad$ Update $\boldsymbol{\Sigma}$ using (10);

5 $\quad$ Update $\mathbf{S}_i$ and $\mathbf{Q}_i$ using (18) and (19);

6 $\quad$ Update γ_i using (24);

7 $\quad$ Update γ_0 using (25);

8 $\quad$ Update $\mathbf{B}_i$ using (20)–(23);

9 $\quad$ $\epsilon = \|\boldsymbol{\mu}_x^{\mathrm{new}} - \boldsymbol{\mu}_x\|_F / \|\boldsymbol{\mu}_x^{\mathrm{new}}\|_F$;

10 $\quad$ $\vartheta = \vartheta + 1$.

11 **end**

Output : $\hat{\boldsymbol{\sigma}} = \boldsymbol{\Psi}\hat{\boldsymbol{\mu}}$

and 30 mm. The background substance in this test was 0.1% (w/v) salt solution, whose conductivity was 0.2 ± 0.001 S/m throughout the frequency range measured. Multi-frequency voltage measurements of a chopped carrot cylinder and an electrically insulating nylon rod were collected at different frequencies varying from 10 KHz to 300 KHz. The measured bioimpedance spectrum of the carrot cylinder using an impedance analyzer is given in Fig. 2(c). The selection of the stimulation frequency was based on the three dispersion mechanisms [24], [25], which illustrated the frequency response of biological materials. 20–100 KHz is located within the β-dispersion, where the conductivity variation of the materials is mainly attributed to the interfacial polarization due to the existence of the insulating membrane surrounding the cells. The evaluation of electrical properties within this range is useful for many industrial applications such as food quality control. The diameter of the carrot cylinder and nylon rod are approximately 25 mm and 30 mm. The finite element method (FEM) is employed to numerically solve the EIT inverse problem. The FEM mesh adopted in this paper is provided in Fig. 2(b). The FEM mesh is provided in Fig. 2(b). As we can see from Fig. 2(b), a total of $N = 812$ square simplices constitute the senor domain with an approximate circular boundary, and the diameter consists of 32 pixels. As such, the size of each pixel is approximately $15.11\,\mathrm{mm}^2$.

Remark 2: Salt solution is among the most commonly used background substances in the EIT tank experiments (See, e.g., [26], [27]). By adjusting the saline hydrolysis concentration, its conductivity can be flexibly regulated to mimic the backgrounds in various industrial/biomedical applications, such as multi-phase flow and cell culture medium. Additionally, salt solution provides a homogeneous background so that the performance of different algorithms can be directly compared and the modelling errors are negligible. It is noteworthy that complex background substances such as cucumber, potato, and banana mashes have also been utilized in some studies [28], [29]. Those backgrounds exhibit reasonable permittivities
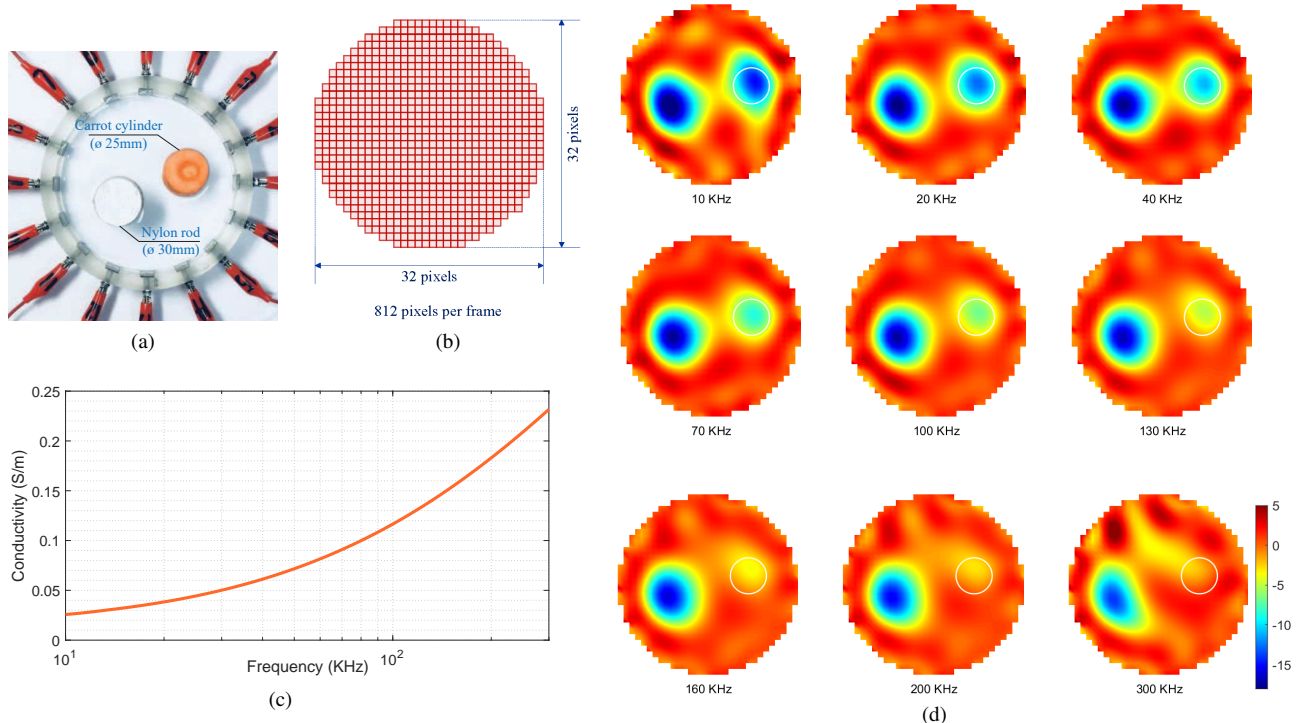

Fig. 2. Phantom experiment settings. (a) Experimental EIT measurement system. (Adapted from Fig. 27 of [23]. Reuse with the permission from IEEE and the authors.) (b) Inverse mesh consisting of 812 pixels. (c) Conductivity truth of carrot cylinder. (d) Reconstructed tdEIT frames in different frequency channels.

TABLE I
ILLUSTRATIVE EXAMPLES OF FDEIT FRAME RECONSTRUCTION OF A BIOLOGICAL PHANTOM.
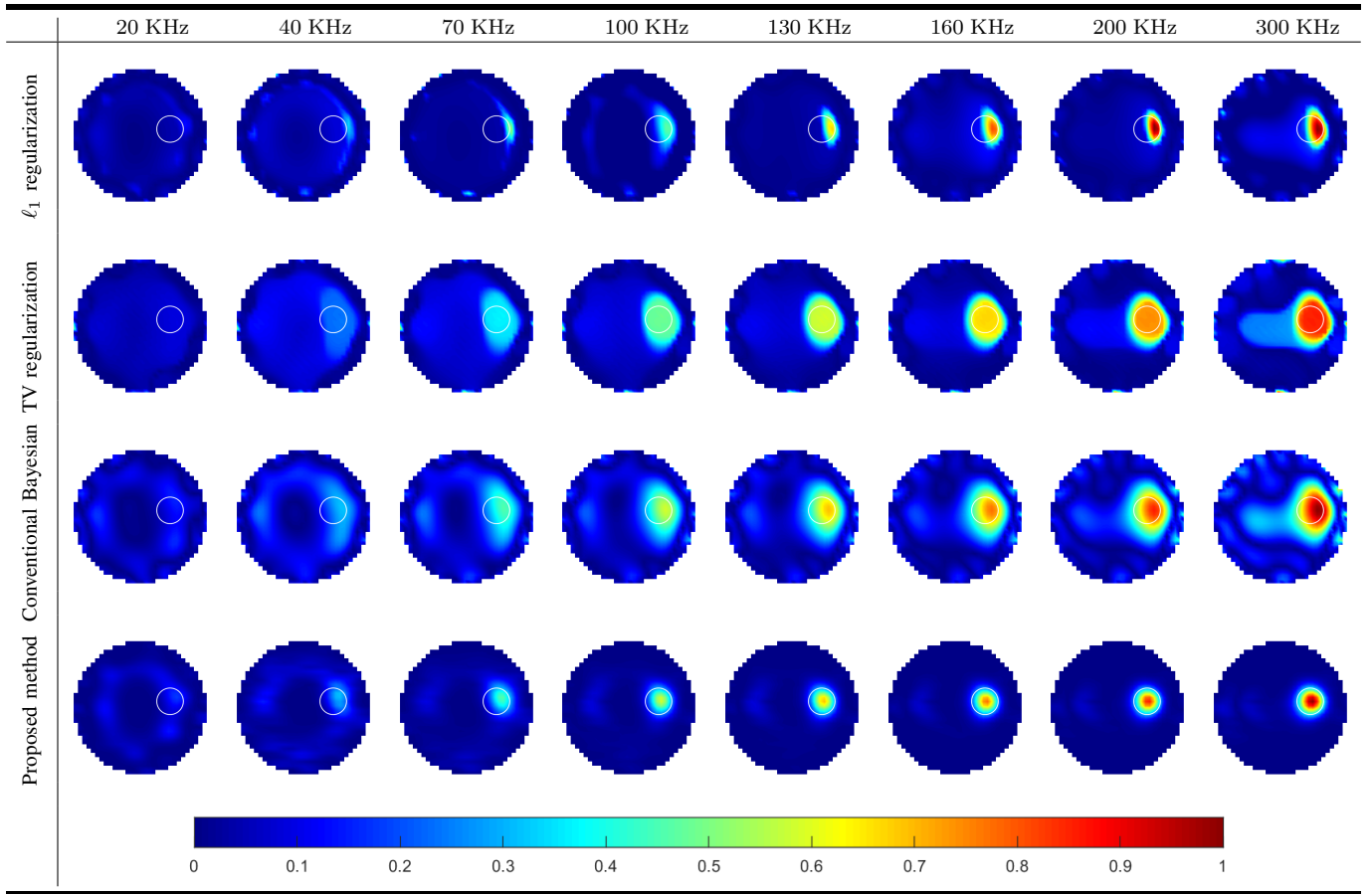
and better simulate certain realistic biomedical scenarios. The induced imaginary part of the background conductivity clearly increases the problem complexity for the inverse solvers. But as the objective of this work is to introduce the MT-SA-SBL algorithm for general fdEIT imaging, we only consider salt solution background. The adoption of complex backgrounds will be investigated in our future work.

As a reference for the fdEIT reconstruction later in this section, Fig. 2(d) shows the reconstructed tdEIT frames of the two phantoms in different frequency channels using the standard Tihonov regularization. Note that in all the following reconstructed tdEIT/fdEIT frames, the approximate region of the carrot cylinder is marked with a white circle to facilitate better demonstration. We can observe from Fig. 2(d) that, the cross-section profiles of the nylon rod remain clear and almost stationary within the frequency range. In contrast, the tdEIT frames of the carrot cylinder gradually become blurred and unidentifiable with the increase of excitation frequency. From the electrical characteristics of the two phantoms shown in Fig. 2(d) it is not difficult to speculate that, the nylon rod will be hardly visible in all the fdEIT frames, while the carrot cylinder will gradually emerge and become more distinct with the increase of frequency.

Table I shows the fdEIT reconstruction results of the phantom, where the voltage data measured at 10 KHz serves as the baseline. Several state-of-the-art methods, including ℓ_1 regularization [30], total variation (TV) regularization [31], and Nissinen's Bayesian method [32], [33], are considered in the comprehensive performance comparison. The target objective parameter in the ℓ_1 regularization is set to 0.1, and the iteration step of the TV regularization is set to 0.01. The iteration termination conditions for the iterative methods are set as $\epsilon_{\min} = 1 \times 10^{-5}$ and $\vartheta_{\max} = 200$. In the absolute imaging mode, reconstructed conductivity values is important. Whereas in difference imaging we are more interested in the contrast of inclusion to background. As such, we follow the common practice [7] to normalize the conductivity values within the range 0 to 1. The fdEIT reconstruction results presented in Table I and our speculation are in a good agreement: The conductivity difference between the target and the baseline increases with frequency. Also, the inter-channel correlation can be directly observed from the reconstruction results, since the variations of pixel amplitudes are small between adjacent frequency channels. The proposed MT-SA-SBL-based EIT inverse solver achieves the best edge/shape preservation performance compared with the reference methods. On the other hand, some artifacts appear near the sensor boundary with the reference methods. In contrast, clear and accurate phantom image with correct anomaly location can be obtained with the proposed MT-SA-SBL approach.
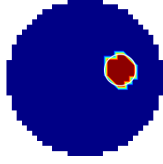
Fig. 3. Generated position truth.

As in this work we attempt to alleviate the inherent low spatial resolution of fdEIT. Customarily, spatial resolution/accuracy of tdEIT is characterized and quantitatively evaluated by metrics such as correlation coefficient and relative reconstruction error [18], [34]. Other commonly used evaluation criteria include figures of merit (FoM) [35], which has been integrated into the EIDORS software package. However, a quantitative evaluation for fdEIT is challenging compared with tdEIT, because the conductivity is changing with frequency and the ground truth is unknown. In this context, to facilitate convenient comparison, we have generated one *position truth* according to the position of the inclusion in Fig. 2(a), which is shown in Fig. 3. Although this position truth does not represent the exact true frequency-dependent conductivity distributions, approximate and objective quantitative evaluation can still be obtained by using the following two measurable metrics [18]:

$$\text{cor} = \frac{\sum_{n=1}^{N} \left(\boldsymbol{\kappa}_n - \bar{\boldsymbol{\kappa}} \right) \left(\boldsymbol{\varsigma}_n - \bar{\boldsymbol{\varsigma}} \right)}{\sqrt{\sum_{n=1}^{N} \left(\boldsymbol{\kappa}_n - \bar{\boldsymbol{\kappa}} \right)^2 \sum_{n=1}^{N} \left(\boldsymbol{\varsigma}_n - \bar{\boldsymbol{\varsigma}} \right)^2}}, \tag{28}$$

and

$$\text{err} = \frac{\| \boldsymbol{\kappa} - \boldsymbol{\varsigma} \|_2}{\| \boldsymbol{\varsigma} \|_2}, \tag{29}$$

where $\boldsymbol{\varsigma}$ and $\boldsymbol{\kappa}$ respectively denote the position truth and the reconstructed image. n represents the n-th pixel. The above two metrics are respectively termed correlation coefficient and the relative reconstruction error.

We can readily see that the former metric measures the similarity between the reconstruction result and the position truth, while the latter one measures the severity of distortions and/or artifacts. However, it is important to keep in mind that, as the conductivity images fade at lower frequencies and the position truth is not the real truth, these two metrics only give a rough assessment in these cases. The performance comparisons with respect to the correlation and error metrics are provided in Figs. 4(a) and (b). The 20 KHz result was discarded since the phantom is completely invisible at such a low frequency. Inspired by the FoM, we also design two complementary metrics for algorithm evaluation, i.e., the contrast accuracy and the shape deformation. The contrast accuracy is formally similar to the amplitude response (AR) in the FoM, which is deigned to compare the amplitudes of

the reconstructed background/anomaly differences.

$$\text{cst} = \frac{\sum_{n \in \mathcal{T}} \boldsymbol{\kappa}_n}{S_{\text{t}} \dfrac{\kappa_{\text{t}} - \kappa_{\text{r}}}{\Delta \kappa_{\text{max}}}}, \tag{30}$$

where S_{t} represents the size of the target area $\mathcal{T}$. κ_{t} and κ_{r} are the conductivities of the target and the reference. $\Delta \kappa_{\text{max}}$ denotes the maximum difference between the target and the reference. From the reconstructed image $\boldsymbol{\kappa}$, a one-fourth amplitude binary image $\boldsymbol{\kappa}_q$ is defined as all pixels exceeding $\frac{1}{4}$ of the image maximum. On this basis, shape deformation is defined to describe fraction of the reconstructed one-fourth amplitude set which does not fit within the shape of the target area:

$$\text{shp} = \frac{\sum_{n \notin \mathcal{T}} [\boldsymbol{\kappa}_{\text{q}}]_n}{\sum_{n} [\boldsymbol{\kappa}_{\text{q}}]_n}, \tag{31}$$

The performance comparisons with respect to the two complementary metrics are shown in Figs. 4(c) and (d). Note that the desired behavior of contrast accuracy metric should be equal to 1, which indicates that the reconstructed background/anomaly difference matches the conductivity truth. Thus, we can tell from Fig. 4(c) that, each method achieves a best amplitude contrast accuracy at a specific frequency and none of them shows an overwhelming advantage with respect to this metric. However, the result of shape deformation analysis suggests an evident superiority of the proposed algorithm, which is quite similar to the result in Fig. 4(b). We can summarize from Figs. 4 that, the proposed method is able to achieve a significantly enhanced fidelity of the phantom shape and it can also yield a remarkably reduced reconstruction error, which tallies with the EIT results in Table I.

Remark 3: The phase value of the measured conductivity is useful for revealing the properties of biological subjects. However, the experiments in this study are mainly designed to compare the performance of different algorithms in general fdEIT image reconstruction, so we only use the magnitude value to reduce the complexity in the sensitivity computation. This is a common practice in many similar studies (See, e.g., [5], [7], [18]). We also feel that accurate estimation of the phase value requires joint optimization of measurement system and the reconstruction algorithm, which is beyond the scope of this paper. We certainly will investigate the phase value of the measured conductivity in our future research.

V. CONCLUSION

In this paper, fdEIT is addressed in the MMV SBL framework for the first time. A novel MT-SA-SBL algorithm was developed for fdEIT exploiting the multiple-task and 2D structure dependencies. The feasibility of the proposed approach is studied through real-data experiments, where significant improvements in terms of spatial resolution and artifact suppression over previous efforts are observed. In addition, by employing the modified MLM approach for MMV model, the computational complexity required is substantially reduced compared with directly applying previously proposed SA-SBL algorithm for each individual frequency channel. Two
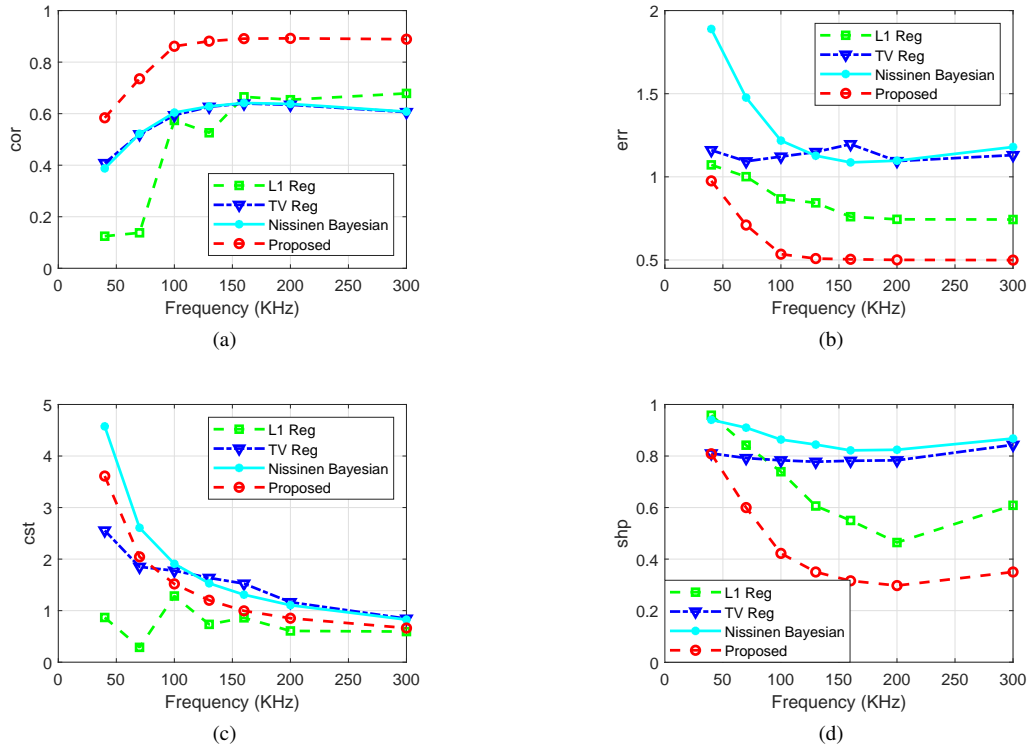
Fig. 4. Quantitative evaluation using objective metrics. (a) Correlation coefficient. (b) Relative reconstruction error. (c) Contrast accuracy. (d) Shape deformation.

objective and quantitative evaluation criteria for fdEIT imaging are also designed in this work. Our future work will focus on accommodating for the complexity of human anatomy for practical clinical application.

REFERENCES

[1] M. Marsousi, K. Plataniotis, and S. Stergiopoulos, "Computer-assisted 3-D ultrasound probe placement for emergency healthcare applications," *IEEE Trans. Ind. Inf.*, vol. 12, no. 4, pp. 1380–1391, Aug. 2016.

[2] Y. Motai, D. Ma, and H. Yoshida, "Smart anomaly prediction in nonstationary CT colonography screening," *IEEE Trans. Ind. Inf.*, vol. 12, no. 6, pp. 2292–2301, Dec. 2016.

[3] B. H. Brown, "Electrical impedance tomography (EIT): a review," *J. Med. Eng. Technol.*, vol. 27, no. 3, pp. 97–108, May 2003.

[4] J. K. Seo, J. Lee, S. W. Kim, and et al., "Frequency-difference electrical impedance tomography (fdEIT): algorithm development and feasibility study," *Physiol. Meas.*, vol. 29, no. 8, pp. 929–944, Aug. 2008.

[5] D. Liu, V. Kolehmainen, and *et al.*, "Nonlinear difference imaging approach to three-dimensional electrical impedance tomography in the presence of geometric modeling errors," *IEEE Trans. Biomed. Eng.*, vol. 63, no. 9, pp. 1956–1965, Sept. 2016.

[6] M. Goharian, M. Soleimani, A. Jegatheesan, and et al., "A DSP based multi-frequency 3D electrical impedance tomography system," *Ann. Biomed. Eng.*, vol. 36, no. 9, pp. 1594–1603, Feb. 2008.

[7] E. Malone, G. S. dos Santos, and D. S. Holder, "Multifrequency electrical impedance tomography using spectral constraints," *IEEE Trans. Med. Imaging*, vol. 33, no. 2, pp. 340–350, Feb. 2014.

[8] G. S. Alberti, H. Ammari, B. Jin, and et al., "The linearized inverse problem in multifrequency electrical impedance tomography," *SIAM J. Imag. Sci.*, vol. 9, no. 4, pp. 1525–1551, Apr. 2016.

[9] S. A. Santos, M. Czaplik, J. Orschulik, and et al., "Lung pathologies analyzed with multi-frequency electrical impedance tomography: Pilot animal study," *Respir. Physiol. Neurobiol.*, vol. 254, pp. 1–9, Aug. 2018.

[10] L. Yang, M. Dai, C. Xu, and et al., "The Frequency Spectral Properties of Electrode-Skin Contact Impedance on Human Head and Its Frequency-Dependent Effects on Frequency-Difference EIT in Stroke Detection from 10Hz to 1MHz," *PloS one*, vol. 12, no. 1, Art. no. e0170563, Jan. 2017.

[11] S. Kim, E. J. Lee, E. J. Woo, and J. K. Seo, "Asymptotic analysis of the membrane structure to sensitivity of frequency-difference electrical impedance tomography," *Inverse Prob.*, vol. 28, no. 7, pp. 075004, July 2012.

[12] A. Adler, and A. Boyle, "Electrical impedance tomography: tissue properties to image measures," *IEEE Trans. Biomed. Eng.*, vol. 66, no. 11, pp. 2494–2504, Nov. 2017.

[13] D. S. Holder, *Electrical Impedance Tomography: Methods, History and Applications*. IOP Publishing, 2006.

[14] J. Jang, and J. K. Seo, "Detection of admittivity anomaly on high-contrast heterogeneous backgrounds using frequency difference EIT," *Physiol. Meas.*, vol. 36, no. 6, pp. 1179–1192, June 2015.

[15] J. Kaipio and E. Somersalo, *Statistical and Computational Inverse Problems*. Springer Science & Business Media, 2006.

[16] A. M. Stuart, "Inverse problems: A Bayesian perspective," *Acta Numerica*, vol. 19, pp. 451–559, May 2010.

[17] Z. Zhang and B. D. Rao, "Extension of SBL algorithms for the recovery of block sparse signals with intra-block correlation," *IEEE Trans. Signal Process.*, vol. 61, no. 8, pp. 2009–2015, Apr. 2013.

[18] S. Liu, J. Jia, Y. D. Zhang, and Y. Yang, "Image reconstruction in electrical impedance tomography based on structure-aware sparse Bayesian learning," *IEEE Trans. Med. Imaging*, vol. 37, no. 9, pp. 2090–2102, Sept. 2018.

[19] S. Liu, H. Wu, Y. Huang, Y. Yang, and J. Jia, "Accelerated structure-aware sparse Bayesian learning for three-dimensional electrical impedance tomography," *IEEE Trans. Ind. Inf.*, vol. 15, no. 9, pp. 5033–5041, Sept. 2019.

[20] S. N. Das, S. Misra, B. E. Wolfinger, and M. S. Obaidat, "Temporal-correlation-aware dynamic self-management of wireless sensor networks," *IEEE Trans. Ind. Inf.*, vol. 12, no. 6, pp. 2127–2138, Dec. 2016.

[21] X. Gu and S. Wang, "Bayesian Takagi-Sugeno-Kang fuzzy model and its joint learning of structure identification and parameter estimation," *IEEE Trans. Ind. Inf.*, vol. 14, no. 12, pp. 5327–5337, Dec. 2018.

[22] Z. Zhang, T. Jung, S. Makeig, and et al., "Spatiotemporal sparse Bayesian learning with applications to compressed sensing of multi-channel physiological signals," *IEEE Trans. Neural Syst. Rehabil. Eng.*, vol. 22, no. 6, pp. 1186–1197, Apr. 2014.

[23] C. Tan, S. Liu, J. Jia, and F. Dong, "A wideband electrical impedance tomography system based on sensitive bioimpedance spectrum bandwidth," *IEEE Trans. Instrum. Meas.*, vol. 69, no. 1, pp. 144–154, Jan. 2020.

[24] H. Schwan, "Electrical properties of tissues and cell suspensions: Mechanisms and models," in *Proc. Annu. Int. Conf. IEEE Eng. Med. Biol. Soc.*, Baltimore, MD, USA, Nov. 1994, pp. A70–A71.

[25] Y. Xu, X. Xie, Y. Duan, L. Wang, Z. Cheng, and J. Cheng, "A review of impedance measurements of whole cells," *Biosens. Bioelectron.*, vol. 77, pp. 824–836, Mar. 2016.

[26] C. Wu and M. Soleimani, "Frequency difference EIT with localization: A potential medical imaging tool during cancer treatment," *IEEE Access*, vol. 7, pp. 21870–21878, Mar. 2019.

[27] M. R. Baidillah, A. S. Iman, Y. Sun, and M. Takei, "Electrical impedance spectro-tomography based on dielectric relaxation model," *IEEE Sens. J.*, vol. 17, no. 24, pp. 8251–8262, Dec. 2017.

[28] E. Malone, G. S. dos Santos, D. S. Holder, and S. Arridge, "A reconstruction-classification method for multifrequency electrical impedance tomography," *IEEE Trans. Med. Imaging*, vol. 34, no. 7, pp. 1486–1497, July 2014.

[29] T. Menden, J. Orschulik, S. Dambrun, and et al., "Reconstruction algorithm for frequency-differential EIT using absolute values," *Physiol. Meas.*, vol. 40, no. 3, art. no. 034008, Mar. 2019.

[30] J. N. Tehrania, A. McEwana, C. Jin, and A. van Schaikb, "$L1$ regularization method in electrical impedance tomography by using the $L1$-curve (Pareto frontier curve)," *Appl. Math. Modell.*, vol. 36, no. 3, pp. 1095–1105, Mar. 2012.

[31] A. Borsic, B. M. Graham, A. Adler, and W. R. Lionheart, "*In vivo* impedance imaging with total variation regularization," *IEEE Trans. Med. Imaging*, vol. 29, no. 1, pp. 44–54, Jan. 2010.

[32] A. Nissinen, L. M. Heikkinen, and J. P. Kaipio, "The Bayesian approximation error approach for electrical impedance tomography — experimental results," *Meas. Sci. Technol.*, vol. 19, no. 1, pp. 015501, Jan. 2008.

[33] H. Li, R. Chen, C. Xu, and et al., "Unveiling the development of intracranial injury using dynamic brain EIT: An evaluation of current reconstruction algorithms," *Physiol. Meas.*, vol. 38, no. 9, pp. 1776–1790, Sept. 2017.

[34] N. Polydorides and H. McCann, "Electrode configurations for improved spatial resolution in electrical impedance tomography," *Meas. Sci. Technol.*, vol. 13, no. 12, pp. 1862-–1870, Nov. 2002.

[35] A. Adler, J. H. Arnold, R. Bayford, and et al., "GREIT: a unified approach to 2D linear EIT reconstruction of lung images," *Physiol. Meas.*, vol. 30, no. 6, pp. S35–S55, June 2009.

Shengheng Liu (S'14–M'17) received the B.Eng. and Ph.D. degrees in electronics engineering from the School of Information and Electronics, Beijing Institute of Technology, China, in 2010 and 2017, respectively.

Dr. Liu is currently an Associate Professor with the School of Information Science and Engineering, Southeast University (SEU), China. Prior to joining SEU, he held a postdoctoral position at the Institute for Digital Communications, The University of Edinburgh, UK, from 2017 to 2018. He also worked as a Visiting Research Associate from 2015 to 2016 at the Department of Electrical and Computer Engineering, Temple University, Philadelphia, PA, USA, under the support of the China Scholarship Council. Dr. Liu is a recipient of the 2017 National Excellent Doctoral Dissertation Award from the China Institute of Communications. His research interests mainly focus on intelligent sensing and communications.

Yongming Huang (M'10–SM'16) received the B.S. and M.S. degrees from Nanjing University, Nanjing, China, in 2000 and 2003, respectively, and the Ph.D. degree in electrical engineering from Southeast University, Nanjing, China, in 2007.

Since 2007, he has been a faculty member with the School of Information Science and Engineering, Southeast University, where he is currently a Full Professor. From 2008 to 2009, he visited the Signal Processing Laboratory, School of Electrical Engineering, Royal Institute of Technology, Stockholm, Sweden. He has authored more than 200 peer-reviewed papers, submitted more than ten technical contributions to the IEEE standards, and hold more than 50 invention patents. His current research interests include MIMO wireless communication, cooperative wireless communication, and millimeter wave wireless communication. He was an Associate Editor for the IEEE TRANSACTIONS ON SIGNAL PROCESSING, IEEE WIRELESS COMMUNICATIONS LETTERS, EURASIP JOURNAL ON ADVANCES IN SIGNAL PROCESSING, and EURASIP JOURNAL ON WIRELESS COMMUNICATIONS AND NETWORKING.

Hancong Wu (S'16–M'19) received his dual B.Eng. (Hons) degree in electronics and electrical engineering from The University of Edinburgh, UK, and the South China University of Technology, Guangzhou, China, in 2015, and Ph.D. degree at the Agile Tomography Group, School of Engineering, The University of Edinburgh, UK, in 2019. He is currently a Postdoctoral Research Associate at the Intelligent Sensing Laboratory, School of Engineering, Newcastle University, UK. His research interests include impedance sensing, electrical tomography, electromyography and prosthesis control.

Chao Tan (M'09–SM'15) received his B.S., M.S., and Ph.D. degrees in control science and engineering from Tianjin University, Tianjin, China, in 2003, 2006, and 2009 respectively.

He has been on the Faculty of the School of Electrical and Information Engineering, Tianjin University since 2009, where he is now a Professor and the Director of the Tianjin International Joint Research and Development Center for Process Imaging and Measurement. Currently, he is also a JSPS Invitational Fellow. His research interests include process parameter detection and control systems, multiphase flow measurement and instrumentation, industrial process tomography and multi-sensor/data fusion.

Jiabin Jia (M'15–SM'19) received the B.Eng. and M.S. degrees in electrical and electronics engineering from the Wuhan University, China, in 2002 and 2005 respectively, and the Ph.D. degree from the University of Leeds, Leeds, UK, in 2010, supported by the Overseas Research Students Award Scheme.

He served as a Hardware Engineer at the H3C Technology Co., Ltd in 2006. He was a Research Fellow in an EPSRC Project for 3 years at the University of Leeds. In 2013, he joined the Institute for Digital Communications, School of Engineering, The University of Edinburgh, Edinburgh, UK, where he is currently a Lecturer in electronic engineering, specializing in agile tomography research. Till now, he has 35 peer-reviewed journal publications and has contributed to and led a range of research projects funded by different funding councils. His current research interests include electrical tomography, acoustic tomography, medical imaging, and industrial process multiphase flow dynamics. His research vision aims at real-time monitoring and innovative diagnostic sensing for medical and industrial applications.